Hepatocellular autophagy modulates the unfolded protein response and fasting-induced steatosis in mice

TITLE

Hepatocellular autophagy modulates the unfolded protein response and fasting-induced steatosis in mice

RUNNING HEAD

Autophagy modulates the UPR and fasting-induced steatosis

AUTHORS

Wilhelmus J. Kwanten[1], Yves-Paul Vandewynckel[2], Wim Martinet[3], Benedicte Y. De Winter[1], Peter P. Michielsen[1,4], Viviane O. Van Hoof[5], Ann Driessen[6], Jean-Pierre Timmermans[7], Pierre Bedossa[8], Hans Van Vlierberghe[2], Sven M. Francque[1,4]

[1] Laboratory of Experimental Medicine and Pediatrics (LEMP), University of Antwerp, Antwerp, Belgium

[2] Department of Hepatology and Gastroenterology, Ghent University, Ghent, Belgium

[3] Laboratory of Physiopharmacology, University of Antwerp, Antwerp, Belgium

[4] Department of Gastroenterology and Hepatology, Antwerp University Hospital, Edegem (Antwerp), Belgium

[5] Department of Clinical Chemistry, Antwerp University Hospital, Edegem (Antwerp), Belgium

[6] Department of Pathology, Antwerp University Hospital/University of Antwerp, Edegem (Antwerp), Belgium

[7] Laboratory of Cell Biology and Histology, University of Antwerp, Antwerp, Belgium.

[8] Department of Pathology, Beaujon Hospital, Assistance Publique-Hôpitaux de Paris, Paris University-Denis Diderot, Clichy, France

CORRESPONDING AUTHOR

Wilhelmus J. Kwanten, MD

University of Antwerp; Laboratory of Experimental Medicine and Pediatrics – Gastroenterology & Hepatology

Universiteitsplein 1, B-2610 Wilrijk, Belgium

E-mail: wilhelmus.kwanten@uantwerpen.be

Telephone : +32 3 265 26 89

Fax : +32 3 265 25 67

WORD COUNT, NUMBER OF FIGURES AND TABLES

- Title: 102 characters
- Short title: 57 characters
- Total word count: 8309 (incl. abstract, new&noteworthy, references, tables legends, figure legends)
    - of which abstract word count: 215/250
- Figures: 5x
- Tables: 3x
- Supporting material:
    Contains 1 figure

CONFLICT OF INTEREST

None to declare

FINANCIAL SUPPORT

WK and SF received funding from the Fund for Scientific Research (FWO) Flanders (11J9513N, 1802154N). HVV is senior clinical investigator of the Research Foundation Flanders. YV is sponsored by a grant from the Special Research Fund (01D20012), Ghent University. The funders had no role in study design, data collection and analysis, decision to publish, or preparation of the manuscript.

AUTHOR CONTRIBUTIONS

WK; study concept and design, acquisition of data, analysis and interpretation of data, statistical analysis, drafting of the manuscript

YV; acquisition of data, analysis and interpretation of data

WM; study concept and design, critical review of the intellectual content

BDW; material support, critical review of the intellectual content

PM; funding, critical review of the intellectual content

VVH; material and technical support, critical review of the intellectual content

AD; interpretation of data

JT; material and technical support, critical review of the intellectual content

PB; interpretation of data

HVV; critical review of the intellectual content

SF; study concept and design, funding, critical review of the intellectual content, supervising of the study

ABSTRACT

BACKGROUND & AIMS

Autophagy and the unfolded protein response (UPR) are key cellular homeostatic mechanisms and are both involved in liver diseases, including non-alcoholic fatty liver disease (NAFLD). Although increasing but conflicting results link these mechanisms to lipid metabolism, their role and potential crosstalk herein has been poorly investigated. Therefore, we assessed the effects of hepatocyte-specific autophagy-deficiency on liver parenchyma, the UPR and lipid metabolism.

METHODS

Adult hepatocellular-specific autophagy-deficient mice (*Atg7*$^{F/F}$*Alb-Cre*$^{+}$) were compared with their autophagy-competent littermates (*Atg7*$^{+/+}$*Alb-Cre*$^{+}$). Livers were analysed by electron microscopy, histology, real-time qPCR and Western blotting.

RESULTS

Atg7$^{F/F}$*Alb-Cre*$^{+}$ mice developed hepatomegaly with significant parenchymal injury as evidenced by inflammatory infiltrates, hepatocellular apoptosis, pericellular fibrosis and a pronounced ductular reaction. Surprisingly, the UPR exhibited a pathway-selective pattern upon autophagy-deficiency. The activity of the adaptive ATF6 pathway was abolished, whereas the pro-apoptotic PERK pathway was increased compared to *Atg7*$^{+/+}$*Alb-Cre*$^{+}$ mice. The IRE1α signal was unaltered. Fasting-induced steatosis was absent in *Atg7*$^{F/F}$*Alb-Cre*$^{+}$ mice. Remarkably, some isolated islands of fat-containing and autophagy-competent cells were observed in these livers.

CONCLUSIONS

Hepatocellular autophagy is essential for parenchymal integrity in mice. Moreover, in case of autophagy-deficiency, the three different UPR branches are pathway-selectively modulated. Attenuation of the ATF6 pathway might explain the observed impairment of fasting-induced steatosis. Finally, autophagy and lipid droplets are directly linked to each other.

NEW AND NOTEWORTHY

This study demonstrates that hepatocellular-specific knock-out of autophagy in mice strongly affects the unfolded protein response (UPR), another essential cellular homeostatic mechanism. Surprisingly these alterations were in a specific pattern, leaving the IRE1α pathway unaltered, while the PERK and ATF6 pathway were respectively induced and reduced. The loss of fasting-induced steatosis in autophagy-deficient mice, might in part be explained by the alterations of the ATF6 pathway.

KEYWORDS

Non-alcoholic fatty liver (NAFLD)

Steatosis

Autophagy

ER stress

Unfolded protein response (UPR)

ABBREVIATIONS (order of appearance)

ATG7	autophagy-related gene 7
UPR	unfolded protein response
ER	endoplasmic reticulum

120	ATF6	activating transcription factor 6
121	PERK	protein kinase RNA-like endoplasmic reticulum (ER) kinase
122	IRE1α	inositol-requiring enzyme-1 α
123	NAFLD	non-alcoholic fatty liver disease
124	NASH	non-alcoholic steatohepatitis
125	GFP-LC3	green fluorescent protein – light chain 3
126	TEM	transmission electron microscopy
127	αSMA	alpha smooth muscle actin
128	ALT	alanine transaminase
129	AST	aspartate transaminase
130	ALP	alkaline phosphatase
131	GGT	gamma-glutamyl transferase
132	ORO	Oil-Red-O
133	SBB	Sudan black B
134	HE	haematoxylin-eosin
135	SREBP-1	sterol regulatory element binding protein 1
136	JNK	JUN N-terminal kinase

INTRODUCTION

Autophagy is a cellular process involved in the breakdown of cytoplasmic contents via a lysosomal pathway. It is constitutively active but can be upregulated by several stressors including metabolic stress (7). Of the three forms of autophagy (macro-, micro- and chaperone-mediated autophagy), macro-autophagy (henceforth autophagy) is considered to be the most important one. During autophagy autophagosomes are formed out of isolation membranes and fuse with lysosomes to enable degradation of their content. Autophagy-related genes (*Atg)* are responsible for the strict control of the autophagic process, with *Atg*7 as an essential mediator for the maturation of autophagosomes (40). Although autophagy was initially regarded as a non-selective process, meanwhile targeted (organelle- or protein-selective) autophagy has also been described (4).

The unfolded protein response (UPR) is another key cellular homeostatic mechanism activated in response to the accumulation of unfolded proteins in the endoplasmic reticulum (ER) (ER stress) (20). ER stress results from perturbation of the normal protein folding capacity of the ER and induces inflammation and oxidative stress (8). The UPR encompasses three major adaptive mechanisms to restore protein homeostasis, named after the respective ER stress sensor: activating transcription factor 6 (ATF6), protein kinase RNA-like ER kinase (PERK) and inositol-requiring enzyme-1α (IRE1α) (20).

Non-alcoholic fatty liver disease (NAFLD), characterized by the accumulation of fat in hepatocytes, has become a leading cause of chronic liver disease in Western countries, with a prevalence of up to 30% (51). When steatosis is accompanied by inflammation and hepatocellular damage, it is called non-alcoholic steatohepatitis (NASH), an entity associated with increased liver- and non-liver-related morbidity and mortality (51). However, the exact mechanisms underlying the development of NASH are incompletely understood (50).

Both autophagy and the UPR are associated with the pathophysiology of NAFLD, amongst other liver diseases (7, 8). Nevertheless, the exact role of autophagy in NAFLD remains controversial (31) and the role of the individual UPR mediators in NAFLD needs to be investigated (16, 56). The UPR is known to promote autophagic flux, however there is increasing evidence of an important crosstalk between autophagy and the UPR (43). Interestingly, impaired autophagy is linked to increased ER stress in steatosis (17, 55). Despite its known involvement in steatosis (6, 42), ATF6-signaling has not yet been investigated in relation to autophagy.

In this study, we investigated the effects of hepatocellular autophagy on the three different branches of the UPR and found important hepatic injury with a significant pathway-selective modulation in autophagy-deficient mice. The occurrence of lipid droplets was directly linked to autophagy, since fasting-induced steatosis was absent in autophagy-deficient mice.

MATERIALS AND METHODS

Animal model

Hepatocellular autophagy-deficient C57Bl/6J mice were developed by crossbreeding homozygous Atg7^{Flox} mice (*Atg7*$^{F/F}$) (28) with mice expressing Cre-recombinase under control of the albumin-promoter as previously described (33). These mice, hereafter denoted as *Atg7*$^{F/F}$*Alb-Cre*$^{+}$, were compared to autophagy-competent littermates that lacked the LoxP vector but expressed the Alb-Cre (*Atg7*$^{+/+}$*Alb-Cre*$^{+}$). To allow *in situ* detection of the autophagy marker LC3, all mice were crossbred with GFP-LC3 transgenic mice (36). Genotyping of the offspring was performed by PCR as described (30, 33).

All mice were kept in a 12:12h light-dark cycle with controlled temperature and humidity and had free access to standard chow (Pavan Service bvba, Oud-Turnhout, Belgium) and water ad libitum. Mice were housed in enriched cages and in accordance with international guidelines.

Adult mice (11-12 weeks of age) were fasted overnight, after which they were weighed and anesthetized with Nembutal® (60 mg/kg i.p.) (Sanofi, Brussels, Belgium). Whole blood samples were obtained by intracardiac puncture. Next, liver and kidneys were removed, random liver samples were fixed in 4% neutral buffered formalin for 24h and dehydrated overnight in 60% isopropanol prior to paraffin embedding. Alternatively, liver tissue was immediately embedded in Richard-Allan Scientific Neg-50 Frozen Section Medium (Thermo Scientific, 6502, Runcorn, UK) using liquid nitrogen and kept at -80ºC. Liver tissue of three animals per group was further processed for transmission electron microscopy, as previously described (34). The remaining liver and kidneys were stored at -80ºC until further processing.

All experiments were approved by the Ethical Committee on Animal Experimentation of the University of Antwerp (ECD 2012/40).

Histology and immunohistochemistry

Sections of paraffin-embedded tissues (5 µm thick) were stained with haematoxylin-eosin (HE), Trichrome-Masson and Picrosirius red according to standard laboratory techniques. Immunohistochemistry was applied using the following primary antibodies (Table 1): anti-alpha smooth muscle actin (αSMA), anti-pan-cytokeratin, anti-ATG7, anti-LC3B and anti-SQSTM1/p62. Secondary antibodies were species-appropriate horseradish peroxidase-conjugates (Vectastain ABC, Vector Laboratories, Burlingame, USA) or in case of LC3B the Envision+ system (K4002, DAKO).

Oil-red-O and Sudan black B staining (O0625 resp. S0395; Sigma-Aldrich) were performed on NEG-50-embedded frozen tissue sections (6 µm thick) according to standard laboratory techniques. Slides were counterstained with Carazzi's haematoxylin.

All samples were blindly assessed by an experienced pathologist (AD) with a detailed recording of all features. The presence of αSMA positive cells is presented as the sum of a semi-quantitative score of each acinar liver zone as follows: 0 = no staining, 1 = staining of some sinusoidal lining cells, occupying <1% of a particular zone, 2 = 1-10%, 3 = 10-30% and 4 = >30% positive sinusoidal lining cells (5). Morphometric measurements of the Picrosirius red and Oil-red-O positive areas were performed using ImageJ software (version 1.46r, NIH) (53). All images were acquired with Universal Grab 6.1 (DCI Labs, Keerbergen, Belgium) using an Olympus BX40 microscope (Tokyo, Japan) and Power HAD Sony 3CCD camera.

Biochemical analysis

Whole blood samples were centrifuged for 15 minutes at 3000 rpm. Plasma was snap frozen in liquid nitrogen and stored at -80ºC. Samples were analysed with an automated Vista 1500 System (Siemens Healthcare Diagnostics, Deerfield, USA) for aspartate aminotransferase (AST), alanine aminotransferase (ALT), gamma-glutamyl transferase (GGT), alkaline phosphatase (ALP), high-density lipoprotein (HDL), low-density lipoprotein (LDL), triglycerides (TG) and glucose. Insulin was determined with an ELISA kit (EZRMI-13K; Millipore, Billerica, USA) according to the manufacturer's instructions. When values were below or above the detection limit for a certain parameter, this value was artificially set to this detection limit.

Western blot and ELISA

Protein samples of the liver were run on a SDS-polyacrylamide gel (Nupage Bis-Tris 4-12%; Life Technologies, Carlsbad, USA) and transferred to a PVDF membrane. Membranes were subsequently blocked in Tris-buffered saline containing 0.05% Tween and 5% non-fat dry milk. Membranes were probed overnight at 4˚C with primary antibody solution with the following antibodies (Table 1): anti-ATG7, anti-SQSTM1/p62, anti-ATF6, anti-CHOP, anti-EIF2α, anti-phospho-eIF2α, anti-GADD34, anti-GRP78, anti-phospho-IRE1α, anti-PDIA4, anti-phospho-PERK, anti-beta-actin and anti-GAPDH. In case of Western Blotting for anti-SREBP-1, the nuclear fraction was extracted (78833; Thermo Scientific, Waltham, USA) and separately loaded on a gel to detect the cleaved protein (loading control for this fraction was performed by imaging of total protein, not shown). After incubation with appropriate horseradish peroxidase secondary antibodies, chemiluminescent signals were obtained with

SuperSignal West Pico (34080; Thermo Scientific) or, in case of anti-LC3B, SuperSignal West Femto Maximum Sensitivity Substrate (34096, Thermo Scientific) using a Lumi-Imager (Roche, Mannheim, Germany). Each lane was loaded with 20-50µg protein and quantitative densitometry values were normalized against beta-actin (LC3B, ATG7, p62) or GAPDH (eIF2α, P-eIF2α). The densitometric analysis was performed using ImageJ. UPR-related antibodies were validated using tunicamycin.

The level of P-JNK was assessed via ELISA (DYC1387B-5; R&D systems Europe Ltd, Abingdon, UK) according to manufacturer's instructions.

In vivo caspase-3 activity

The enzymatic activation of effector caspase-3 was evaluated in liver lysates using the Caspase-3-Glo assay (Promega) following the manufacturer's instructions. Experiments were performed in quadruplicate.

Real-time PCR

Total RNA was extracted from all samples using the RNeasy Mini Kit (Qiagen, Westburg BV, The Netherlands) with on-column DNAse treatment (Qiagen). Needle homogenization was performed. The purity and quantity of total RNA was assessed using spectrophotometry (Nanodrop; Thermo Scientific, Wilmington, USA); samples with a 260:280 ratio between 1.8 and 2.0 were accepted.

One microgram of total RNA was converted to single strand cDNA by reverse transcription (iScript, BioRad, California, USA) with oligo (dT) and random priming. The cDNA was diluted 1/10 and used for real-time quantification using SYBR Green (Sensimix, Bioline Reagents Ltd, London, UK) and 250 nM of each primer. A two-

step program was run on a LightCyclerR 480 (Roche). Cycling conditions were 95°C for 10 minutes and 45 cycles of 95°C for 10 seconds followed by 60°C for 1 minute. Melting curve analysis confirmed primer specificities. All reactions were performed in duplicate. Fold-change expression was calculated using the ΔΔCT method as instructed by Applied Biosystems. The PCR-efficiency of each primer pair was calculated using a standard curve of reference cDNA. Amplification efficiency was determined using the formula $10^{-1/slope}$. The primer set sequences are listed in table 2.

Statistics

All data were analysed by SPSS (version 22, IBM SPSS Statistics software, Armonk NY, USA). Parametric variables were compared using the Student's-t-test, or one-way ANOVA with post-hoc Bonferroni correction whenever appropriate. Non-parametric variables were compared using the Mann-Whitney U test. Figures were created with GraphPad Prism (version 5, GraphPad Software, San Diego CA, USA). Two-tailed probabilities were calculated; p-values <0.05 were considered statistically significant. Data are presented as mean ± SEM.

RESULTS

Autophagy is defective in livers of *Atg7$^{F/F}$Alb-Cre^{+}* mice

The excision of the essential autophagy gene *Atg7* in the livers of *Atg7$^{+/+}$Alb-Cre^{+}* mice (n=16) was demonstrated by western blot showing the elimination of ATG7 and the accumulation of SQSTM1/p62, which is a typical feature of impaired autophagy (data not shown). The opposite was observed in the autophagy-competent mice (*Atg7$^{F/F}$Alb-Cre^{+}*, n=11). Kidneys, used as control for tissue-specificity, expressed comparable ATG7 levels in all mice.

Subsequent immunohistochemical analysis of liver sections reconfirmed the accumulation of p62 positive aggregates in *Atg7$^{F/F}$Alb-Cre^{+}* mice, as well as a lack of fine LC3B positive punctae representative of autophagosomes (data not shown). However, *Atg7$^{F/F}$Alb-Cre^{+}* mice showed large LC3B-positive globular structures, not punctae, predominantly in the pericentral regions. These observations represent the staining of the unconjugated GFP-bound LC3-I protein, which can be incorporated in protein aggregates in an autophagy-independent way (29, 33, 41).

Finally, transmission electron microscopy (TEM) demonstrated absence of autophagic vacuoles in the vast majority of the hepatocytes of *Atg7$^{F/F}$Alb-Cre^{+}* mice, whilst still present in the hepatocytes of *Atg7$^{+/+}$Alb-Cre^{+}* mice. Furthermore, we observed accumulation of deformed mitochondria (Fig. 1A-B). Of note, autophagy was rarely seen in some cells of *Atg7$^{F/F}$Alb-Cre^{+}* mice, as discussed in detail below.

Al together, these data validate hepatocyte-specific deficiency of autophagy in the

Atg7$^{F/F}$*Alb-Cre*$^{+}$ mice.

Hepatocellular autophagy-deficiency causes severe hepatomegaly and pronounced parenchymal damage

Although body weight of *Atg7*$^{F/F}$*Alb-Cre*$^{+}$ mice and *Atg7*$^{+/+}$*Alb-Cre*$^{+}$ controls was comparable (Fig. 2A), *Atg7*$^{F/F}$*Alb-Cre*$^{+}$ mice displayed severe hepatomegaly as reflected by a five-fold increase in the liver-to-body weight ratio ($p<0.001$) compared to *Atg7*$^{+/+}$*Alb-Cre*$^{+}$ mice (Fig. 2B-C). Macroscopically, these enlarged livers exhibited an intense red-brownish colour and had a more solid consistency compared to the livers of *Atg7*$^{+/+}$*Alb-Cre*$^{+}$ mice. Yet the general well-being of *Atg7*$^{+/+}$*Alb-Cre*$^{+}$ mice did not seem to be hampered by their hepatomegaly. Macroscopic abnormalities (e.g. tumours) could not be observed in the *Atg7*$^{F/F}$*Alb-Cre*$^{+}$ mice and spontaneous deaths did not occur.

Microscopically, the liver architecture of *Atg7*$^{F/F}$*Alb-Cre*$^{+}$ mice was severely damaged (Fig. 3A). The hepatocytes were hypertrophic, presented ballooning and frequently displayed a more dense eosinophilic cytoplasm compatible with a pre-apoptotic state, which is in line with the sporadic presence of apoptotic bodies. These findings are indicative of severe hepatocellular injury. Reticulin staining demonstrated the disruption of liver trabeculae (Fig. 3A). Moreover, *Atg7*$^{F/F}$*Alb-Cre*$^{+}$ livers had fine pericellular collagen deposits, as shown by Picrosirius red stain. Morphometrical measurements of the Picrosirius red-positive area showed a significantly higher collagen content in *Atg7*$^{F/F}$*Alb-Cre*$^{+}$ mice than in *Atg7*$^{+/+}$*Alb-Cre*$^{+}$ mice ($p<0,01$, Fig. 3B), although septa or bridging fibrosis could not be observed. Since activated hepatic stellate cells are considered to be the main source of collagen production

(14), an αSMA staining was performed (Fig. 3C). The αSMA score was significantly increased in all acinar zones in *Atg7*$^{F/F}$*Alb-Cre*$^{+}$ mice compared to *Atg7*$^{+/+}$*Alb-Cre*$^{+}$ mice (Fig. 3D). Furthermore, the cellularity prominently increased in *Atg7*$^{F/F}$ *Alb-Cre*$^{+}$ mice. These cells were organized in a string pattern with sometimes tubular-like structures (Fig. 3E). This pattern is consistent with a pronounced ductular reaction (i.e. the proliferation of hepatic progenitor cells) as confirmed by a pan-cytokeratin stain (27). The increased cellularity was also partly due to inflammation with the infiltration of lymphoid cells, as demonstrated by CD3 staining (Fig. 3F).

In line with the microscopic findings, transaminases (ALT, AST) and canalicular tests (ALP, GGT) were significantly increased in *Atg7*$^{F/F}$*Alb-Cre*$^{+}$ mice, both endorsing the hepatocellular injury (Table 3).

Together, autophagy-deficiency appears to be detrimental to the liver, as shown by significant parenchymal injury, pericellular fibrosis and a ductular reaction.

Hepatocellular autophagy-deficiency triggers pathway-selective UPR modulation with a pro-apoptotic pattern

Because autophagy-deficiency could lead to ER stress due to the accumulation of misfolded proteins and impairment of ER turnover (43), different UPR pathways were investigated. Tunicamycin-treated cells, which successfully develop ER stress by inhibition of the N-linked glycosylation of proteins (38), served as a positive control in the analyses of UPR (data not shown).

The glucose-regulated protein, 78kDa (GRP78, also known as BiP) acts as a major sensor of unfolded proteins in the ER. Uncoupling of GRP78 of ATF6, PERK or IRE1α leads to subsequent activation of the respective pathways (20). Both mRNA and protein levels of GRP78 were decreased in *Atg7$^{F/F}$Alb-Cre^{+}* (Fig. 4A, 4E).

The transcription of the chaperones *Pdia4, Herpud1, Grp78, Grp94 and calreticulin,* predominantly regulated by the ATF6-pathway (45), was reduced in *Atg7$^{F/F}$Alb-Cre^{+}* mice, whilst the expression of *Atf6* mRNA itself was unaltered (Fig. 4A). Decreased expression of *Pdia4* was confirmed at the protein level by Western blot (Fig. 4E). Interestingly, the levels of the active (i.e. cleaved) form of ATF6 were robustly decreased in *Atg7$^{F/F}$Alb-Cre^{+}* mice as compared to *Atg7$^{+/+}$Alb-Cre^{+}* mice (Fig. 4E), further confirming the diminished activation of the cytoprotective ATF6 pathway upon autophagy-deficiency. Both ATF6 and the sterol response element binding proteins (SREPB) depend on COPII-transporter vesicles for transport to the Golgi, where cleavage takes place (15, 54). The demonstration of cleaved SREBP-1 in *Atg7$^{+/+}$Alb-Cre^{+}* mice would support the possibility of an interrupted COPII-mediated transporting in *Atg7$^{F/F}$Alb-Cre^{+}* mice. While the levels of uncleaved SREBP-1 were similar, remnants of cleaved SREBP-1, as these levels rapidly decrease when fasted, could not be detected in the nuclear fraction (Fig. 4E-F).

In contrast with ATF6, there was a strong activation of the pro-apoptotic PERK pathway as shown by increased phosphorylation of eIF2α (4E, 4G) and increased mRNA and protein levels of CHOP (Fig. 4B, 4E). Even though it is known that eIF2α can be phosphorylated by other kinases as well, each related to a specific stimulus (12), direct detection of phosphorylated PERK can be troublesome (48) and was

unsuccesful (results not shown). The mRNA and protein levels of *Gadd34,* providing a negative feedback to limit the translational break mediated by p-eIF2α, were unaltered (Fig. 4B, 4E). Because CHOP is a central effector of UPR-mediated apoptosis and increased cell apoptosis was suspected on liver histology (Fig. 3A), hepatic executioner caspase-3 activity was determined and shown to be significantly elevated in *Atg7$^{F/F}$Alb-Cre^{+}* mice ($p<0.01$, Fig. 4C).

Finally, the mRNA expression of IRE1α, the phosphorylation of IRE1α and the IRE1α-mediated splicing of XBP1 mRNA were unaltered in *Atg7$^{F/F}$Alb-Cre^{+}* mice (Fig. 4D). In line with these findings, also the other downstream targets of the IRE1α-XBP1 pathways *(Erdj4, Calnexin)* were unaltered in *Atg7$^{F/F}$Alb-Cre^{+}* mice compared to their controls (Fig. 4D). Besides XBP1-splicing, IRE1α is also able to activate the 'alarm stress' JUN N-terminal kinase (JNK) pathway (19). Hence, the activation of JNK was assessed by ELISA, and found to be lower in *Atg7$^{F/F}$Alb-Cre^{+}* compared to *Atg7$^{+/+}$Alb-Cre^{+}* mice (0.59±0.07 resp. 1.38±0.26 ng/mg protein; $p<0.01$), supporting that IRE1α is not activated upon autophagy-deficiency.

These results demonstrate that the UPR pathways in the liver were selectively modified by autophagy-deficiency, as evidenced by a diminished ATF6 pathway and an enhanced pro-apoptotic PERK pathway.

Hepatocellular autophagy-deficiency leads to absence of fasting-induced steatosis, an improved plasma lipid profile and reduced glycemia

In case of chronic ER stress, loss of ATF6 prevents the development of fatty liver (6). Hence, considering the observed reduction in the ATF6 signalling and given the

debated role of autophagy in steatosis (31), the effects on fasting-induced steatosis were investigated.

Fasting-induced steatosis is a well-known phenomenon caused by the accumulation of large amounts of triglycerides in hepatocytes after fasting for 6-24h (18). This form of steatosis was demonstrated in *Atg7*$^{+/+}$*Alb-Cre*$^{+}$ mice as shown via Oil-red-O (ORO) staining, whereas *Atg7*$^{F/F}$*Alb-Cre*$^{+}$ mice had a significantly lower ORO positivity in their liver parenchyma ($p<0.001$, Fig. 5A, 5B). The absence of the typical fasting-induced steatosis in *Atg7*$^{F/F}$*Alb-Cre*$^{+}$ mice was subsequently verified with a Sudan-black-B stain (SBB) (Fig. 5A). On TEM images, lipid droplets were easily recognized in *Atg7*$^{+/+}$*Alb-Cre*$^{+}$ livers (Fig. 2A). Occasionally, we also observed lipophagy (i.e. the inclusion of lipid droplets in the autophagosomes) in *Atg7*$^{+/+}$*Alb-Cre*$^{+}$ mice. In contrast, lipid droplets or autophagic vacuoles were lacking in the vast majority of *Atg7*$^{F/F}$*Alb-Cre*$^{+}$ hepatocytes (Fig. 2B).

Not only hepatocellular lipid content was altered, also the plasma lipids concentrations were markedly changed. *Atg7*$^{F/F}$*Alb-Cre*$^{+}$ mice demonstrated a significant increase in total cholesterol, which can be attributed to a doubling of both plasma HDL and LDL cholesterol levels (Table 3). In absolute values the amount of HDL was substantially higher than that of LDL in *Atg7*$^{F/F}$*Alb-Cre*$^{+}$ mice. Still, the LDL/HDL ratio was unaltered compared to *Atg7*$^{+/+}$*Alb-Cre*$^{+}$ mice. Plasma triglyceride levels were significantly lower in *Atg7*$^{F/F}$*Alb-Cre*$^{+}$ mice ($p<0.001$, table 3). Additionally, fasting glycemia was lower in *Atg7*$^{F/F}$*Alb-Cre*$^{+}$ mice, while fasting insulinemia was unaltered.

In summary, autophagy-deficiency hampers fasting-induced steatosis in the liver, increases plasma cholesterol levels with a conserved LDL/HDL-ratio, and reduces plasma triglycerides and glycemia.

Lipid-containing and autophagy-competent hepatocytes may occur in *Atg7$^{F/F}$Alb-Cre^{+}* mice

Remarkably, a number of atypical ORO-positive areas were observed in the livers of *Atg7$^{F/F}$Alb-Cre^{+}* mice in the absence of fasting-induced steatosis, which could be confirmed in a SBB stain (Fig 5C). These mixed micro- and macrovesicular fat-positive cell groups did not have a particular zonal distribution and were not observed in *Atg7$^{+/+}$Alb-Cre^{+}* mice. Moreover, the presence of these areas on consecutive sections and on two different fat stainings, argued against an artefact.

Because these cells might potentially represent autophagy-competent cells of unknown origin, an additional stain for ATG7 was performed (Fig. 5D), confirming the effective knock-out of *Atg7* in the hepatocytes of *Atg7$^{F/F}$Alb-Cre^{+}* mice. Remark that the ductular reaction stains as well negative, as it originates out of hepatic progenitor cells (which already expressed albumin), whereas the other non-hepatic cells are positive (Fig. 5D). There were no ATG7 positive cells mimicking the fat-positive cell groups. Cells with a darker appearance tended to correspond to (pro-)apoptotic cells upon HE-staining and are likely the result of condensation of the cytoplasm. Neither LC3B nor p62 stains revealed cells similar to the fat-positive groups.

Intriguingly, our TEM results also revealed sparse fat-containing hepatocytes in *Atg7$^{F/F}$Alb-Cre^{+}* mice. These cells not only contained lipid droplets, but also showed

signs of autophagy, in contrast to the majority of the hepatocytes in which neither autophagy nor lipid droplets were observed. These TEM findings are in line with the occurrence of autophagy-competent hepatocytes in the livers of *Atg7*$^{F/F}$*Alb-Cre*$^{+}$ mice and underline the close connections of lipid droplets and autophagy.

DISCUSSION

In this study, we demonstrate the deleterious consequences of hepatocyte-specific autophagy-deficiency in relation to the different UPR pathways and the concomitant effects on hepatic and serum lipids.

Hepatocyte-specific knock-out of autophagy causes a severe hepatomegaly and hepatic injury as already partially reported in other studies (22, 25, 28, 32, 37, 47, 49). This injury encompasses distortion of the liver architecture, increased apoptosis, general inflammation, activation of hepatic stellate cells, corresponding pericellular fibrosis and a prominent ductular reaction. The latter was also mentioned in a study with Atg5 knock-out mice (37), but was not specifically confirmed using immunohistochemistry. We assume that this ductular reaction can be interpreted as a type 3 ductular reaction (9), i.e. the proliferation of hepatic progenitor cells as an adaptive response to the loss of parenchymal cells and their function. It also implies that the liver is still capable of an adequate compensatory regeneration reaction in case of hepatocyte-specific autophagy-deficiency. However, as albumin is co-expressed in these cells, autophagy will be knocked-out already (Fig. 5D) and hence the injured parenchymal cells will not be replaced by autophagy-competent hepatocytes from this source.

Although the ER stress-activated UPR is known to induce autophagy, the knowledge of the impact of autophagy on the UPR is currently limited (43). Our study demonstrates a significant alteration of the hepatic UPR pattern in conditions of autophagy-deficiency. Moreover, autophagy-deficiency apparently did not lead to a general induction of the UPR, but rather had a selective effect on the distinct UPR

pathways: the IRE1α pathway was unaltered, the ATF6 pathway was attenuated, and the PERK pathway was strongly activated upon autophagy-deficiency. In line with our results, Ni *et al*. (37) did not observe any changes in the IRE1α pathway, but in contrast to our findings and those of Yang *et al.* (55), they did not observe an activation of the PERK pathway either. Since PERK is known to mediate the transcription of many autophagy-related genes and activates autophagic flux (43), its activation may be a compensatory attempt to restore autophagy. The synchronous activation of the PERK-CHOP axis, resulting in enhanced cell apoptosis, is an important but deleterious side effect of this activation. IRE1α is able to stimulate additional cell signalling pathways, amongst them the JNK pathway. This 'alarm stress' pathway is able to induce apoptosis and may stimulate autophagy as well (19, 52). In line with the unstimulated XBP1-splicing, phosphorylation of JNK was reduced in $Atg7^{F/F}AlbCre^{+}$ mice as well. Although seemingly contradictory with the results of the PERK-pathway and the observed apoptosis, the mechanism of actions in the paradigm of adaptive vs. apoptotic phases of these alternative pathways of the UPR remain not well understood (20). Moreover, the overall findings of the UPR pathways might rather point towards 'exhaustion' of the proteins and adaptive capacities of the UPR, thus the transition towards UPR-induced cell death.

To the best of our knowledge, the present study is the first to report effects of autophagy on the ATF6 pathway in mice. ATF6 is a transmembrane protein localized in the ER that has to be transported to the Golgi-complex, where it is cleaved to form an active transcription factor, which in turn regulates genes responsible for protein folding, proteasomal degradation of misfolded proteins (ERAD) and genes supporting the XBP1 pathway (20). How exactly autophagy inhibits the ATF6 pathway remains

unclear, yet the COPII complex might be involved as our results showed that cleaved ATF6 but not total ATF6 was diminished in the liver of *Atg7*$^{F/F}$*Alb-Cre*$^{+}$ mice. Levels of SREBP-1 were not supportive for this hypothesis as cleaved nuclear SREBP-1 becomes already undetectable after 6h fasting (21). Accordingly, potential differences in the cleavage of SREBP-1 could not be detected. The COPII complex not only transports ATF6 to the Golgi complex, but is also involved in the ER-Golgi intermediate compartment and in LC3-lipidation (15). Hence, interruption of the formation of LC3-II in order to abolish autophagy might interfere with these complexes and prevent ATF6 transport to the Golgi apparatus, hence its activation.

Interestingly, autophagy-deficiency not only had detrimental effects on the liver, but also caused notable effects on the lipid metabolism. Autophagy appears to be necessary for the development of the physiological fasting-induced steatosis, which is no longer present in autophagy-deficient mice. These results are in contrast with augmented steatosis after fasting as reported by Singh *et al.* (46). However, even with the observation of lipophagy, our results are in line with earlier observations (25, 32, 33, 44), conflicting results about the exact role of autophagy in lipid metabolism have also been reported for other models of fatty liver (26, 31) and might be explained by minor differences in experimental protocols, the context-dependent behaviour of autophagy and the interaction with other important metabolic body compartments like visceral fat or muscle tissue (26, 31).

The question arises whether the observed effects on the lipid metabolism in autophagy-deficient mice are causally related to the observed UPR pattern. Acute ER stress has been shown to stimulate liver steatosis rather than alleviating it.

552 However, genetic ablation of the different UPR pathways does not prevent steatosis,
553 indicating that the combined action of UPR pathways, rather than a single isolated
554 pathway, is responsible for fat accumulation (42). Autophagy-deficiency causes a
555 sustained interruption of cellular homeostasis, pointing to chronic rather than acute
556 ER stress. Ablation of ATF6 in case of chronic, but not acute, ER stress has been
557 shown to prevent fatty liver (6). This effect of ATF6 in chronic conditions might at
558 least partially explain the observed loss of fasting-induced steatosis.
559
560 The importance of autophagy in cellular lipid metabolism is underlined by the finding
561 of fat-containing cells in livers of *Atg7*$^{F/F}$*Alb-Cre*$^{+}$ mice (Fig. 5C) in a pattern that is
562 clearly distinct from fasting-induced steatosis. These cells were more evident after
563 staining with SBB, which is known to stain a broader spectrum of fats (2), suggesting
564 that these vacuoles may contain another type of fat (i.e. glycolipids or cholesterol).
565 However, glycolipids are unlikely given a negative Periodic Acid-Schiff reaction (data
566 not shown). Intriguingly, TEM revealed the co-occurrence of lipid droplets and
567 autophagic vacuoles in some hepatocytes of *Atg7*$^{F/F}$*Alb-Cre*$^{+}$ mice, similar to
568 *Atg7*$^{+/+}$*Alb-Cre*$^{+}$ mice. This finding is indicative of the existence of autophagy-
569 competent hepatocytes in *Atg7*$^{F/F}$*Alb-Cre*$^{+}$ mice.
570
571 Potential explanations for the presence of rare clusters of autophagy-competent cells
572 in *Atg7*$^{F/F}$*Alb-Cre*$^{+}$ mice include the escape of ablation by Cre-recombinase (10) or
573 repopulation of the liver by newly developed autophagy-competent hepatocytes that
574 have not expressed albumin yet and are therefore still autophagy-competent (10, 23).
575 The latter explanation is more likely, since albumin has been found to be expressed
576 in hepatocytes early during embryogenesis and hepatic progenitor cells already

express albumin (24, 35). Despite the occasional presence of fat droplets and autophagosomes on TEM in *Atg7*$^{F/F}$*Alb-Cre*$^{+}$ mice, these atypical cells are negative for the ATG7 stain, and their fat content does not seem to be identical to that of *Atg7*$^{+/+}$*Alb-Cre*$^{+}$ hepatocytes. We hypothesize that albumin (thus also Cre-recombinase) becomes expressed during the maturation of these albumin-naive pre-hepatocytes to adult hepatocytes. This gradual change will ultimately lead to the knock-out of *Atg7.* The current and unusual appearance of the lipid droplets in these cells might be a simple consequence of this transformation. Previously formed lipid droplets could be in a weaning state, while the absence of autophagy hinders the maintenance or *de novo* formation of lipid droplets by as yet unclarified mechanisms.

Autophagy-deficiency not only affected the lipid content of the hepatocytes, but also had a clear impact on serum lipids with reduced triglycerides levels and increased levels of HDL and LDL cholesterol. Although, the latter was a balanced increase without affecting their relative proportions. Ma *et al.* (32) also reported that serum triglycerides were decreased in control fed conditions, but not in high fat diet conditions. However, they did not report on other serum lipids. Additional reports on serum lipids in relation to hepatocyte-specific autophagy-deficiency are lacking. Lower triglyceride production (25) and VLDL production (32) upon autophagy knock-out have been reported, which might explain the lower plasma triglycerides, but not the higher HDL and LDL levels observed in present study. Furthermore, neither of these findings explains the absence of hepatocellular fat. The absence of both hepatocellular and serum triglycerides in hepatocellular autophagy-deficiency might point to an increased oxidation of fatty acids and/or the inability to incorporate them in triglycerides. Mitochondria play a central role in cellular homeostasis, and are

removed by non-selective autophagy or selectively by so-called ‘mitophagy’ (11). The observed accumulation of misformed mitochondria implies mitochondrial dysfunction that has previously been linked to impaired steatosis in autophagy-deficient mice via the production of FGF21, leading to increased oxidation outside the liver, despite a reduced oxidative phosphorylation (25). Autophagy also prevents the activation of caspase-8 and the mitochondrial death pathway (1), as well is defective mitophagy involved in cell injury (11). Further, in depth analysis of the mitochondrial dysfunction, given its central role in the pathophysiology of NAFLD (3), related to autophagy-deficiency would be of specific interest for further study.

In conclusion, this study shows that the parenchymal integrity of the liver depends on hepatocellular autophagy, since autophagy-deficiency results in injury, inflammation and apoptosis. The reciprocal but pathway-selective effects of autophagy on ER stress and the UPR at least partially explain the observed effects. More specifically, the ATF6 pathway might account for the observed impairment of fasting-induced steatosis, in addition to the direct linkage between autophagy and lipid droplets. Hence, autophagy and pathway-selective UPR modulation may become relevant targets in the treatment of NAFLD.

ACKNOWLEDGEMENTS

The authors thank the staff of the laboratory of experimental medicine and pediatrics (LEMP) of the University of Antwerp and Mrs Eliene Bogaerts of the Ghent University for their practical assistance as well as Mrs Rita van den Bossche and Dr Isabel Pintelon (University of Antwerp) for assistance with histology and electron microscopy.

REFERENCES

1. **Amir M**, **Zhao E**, **Fontana L**, **Rosenberg H**, **Tanaka K**, **Gao G**, **Czaja MJ**. Inhibition of hepatocyte autophagy increases tumor necrosis factor-dependent liver injury by promoting caspase-8 activation. *Cell Death Differ* 20: 878–87, 2013.

2. **Bayliss High O**. *Lipid Histochemistry (Royal Microscopical Society Microscopy Handbooks)*. Oxford: Oxford University Press, 1984.

3. **Begriche K**, **Massart J**, **Robin M-A**, **Bonnet F**, **Fromenty B**. Mitochondrial adaptations and dysfunctions in nonalcoholic fatty liver disease. *Hepatology* 58: 1497–507, 2013.

4. **Choi AMK**, **Ryter SW**, **Levine B**. Autophagy in human health and disease. *N Engl J Med* 368: 651–62, 2013.

5. **Chu C-M**, **Shyu W-C**, **Liaw Y-F**. Comparative studies on expression of alpha-smooth muscle actin in hepatic stellate cells in chronic hepatitis B and C. *Dig Dis Sci* 53: 1364–9, 2008.

6. **Cinaroglu A**, **Gao C**, **Imrie D**, **Sadler KC**. Activating transcription factor 6 plays protective and pathological roles in steatosis due to endoplasmic reticulum stress in zebrafish. *Hepatology* 54: 495–508, 2011.

7. **Czaja MJ**, **Ding W-X**, **Donohue TM**, **Friedman SL**, **Kim J-S**, **Komatsu M**, **Lemasters JJ**, **Lemoine A**, **Lin JD**, **Ou JJ**, **Perlmutter DH**, **Randall G**, **Ray RB**, **Tsung A**, **Yin X-M**. Functions of autophagy in normal and diseased liver. *Autophagy* 9: 1131–58, 2013.

8. **Dara L**, **Ji C**, **Kaplowitz N**. The contribution of endoplasmic reticulum stress to liver diseases. *Hepatology* 53: 1752–1763, 2011.

9. **Desmet VJ**. Ductal plates in hepatic ductular reactions. Hypothesis and implications. I. Types of ductular reaction reconsidered. *Virchows Arch* 458: 251–9, 2011.

10. **Diaz F**, **Garcia S**, **Hernandez D**, **Regev A**, **Rebelo A**, **Oca-Cossio J**, **Moraes CT**. Pathophysiology and fate of hepatocytes in a mouse model of mitochondrial hepatopathies. *Gut* 57: 232–42, 2008.

11. **Ding W-X**, **Yin X-M**. Mitophagy: mechanisms, pathophysiological roles, and analysis. *Biol Chem* 393: 547–64, 2012.

12. **Donnelly N**, **Gorman AM**, **Gupta S**, **Samali A**. The eIF2α kinases: their structures and functions. *Cell Mol Life Sci* 70: 3493–511, 2013.

13. **Espenshade PJ**. SREBPs: sterol-regulated transcription factors. *J Cell Sci* 119: 973–6, 2006.

14. **Friedman SLS**. Hepatic stellate cells: protean, multifunctional, and enigmatic cells of the liver. *Physiol Rev* 88: 125–72, 2008.

15. **Ge L**, **Zhang M**, **Schekman R**. Phosphatidylinositol 3-kinase and COPII generate LC3 lipidation vesicles from the ER-Golgi intermediate compartment. *Elife* 3: e04135, 2014.

16. **Gentile CL**, **Frye M**, **Pagliassotti MJ**. Endoplasmic reticulum stress and the

unfolded protein response in nonalcoholic fatty liver disease. *Antioxid Redox Signal* 15: 505–21, 2011.

17. **González-Rodríguez A**, **Mayoral R**, **Agra N**, **Valdecantos MP**, **Pardo V**, **Miquilena-Colina ME**, **Vargas-Castrillón J**, **Lo Iacono O**, **Corazzari M**, **Fimia GM**, **Piacentini M**, **Muntané J**, **Boscá L**, **García-Monzón C**, **Martín-Sanz P**, **Valverde ÁM**. Impaired autophagic flux is associated with increased endoplasmic reticulum stress during the development of NAFLD. *Cell Death Dis* 5: e1179, 2014.

18. **Guan H-P**, **Goldstein JL**, **Brown MS**, **Liang G**. Accelerated fatty acid oxidation in muscle averts fasting-induced hepatic steatosis in SJL/J mice. *J Biol Chem* 284: 24644–24652, 2009.

19. **Hetz C**, **Glimcher LH**. Fine-tuning of the unfolded protein response: Assembling the IRE1alpha interactome. *Mol Cell* 35: 551–61, 2009.

20. **Hetz C**. The unfolded protein response: controlling cell fate decisions under ER stress and beyond. *Nat Rev Mol Cell Biol* 13: 89–102, 2012.

21. **Horton JD**, **Bashmakov Y**, **Shimomura I**, **Shimano H**. Regulation of sterol regulatory element binding proteins in livers of fasted and refed mice. *Proc Natl Acad Sci U S A* 95: 5987–92, 1998.

22. **Inami Y**, **Waguri S**, **Sakamoto A**, **Kouno T**, **Nakada K**, **Hino O**, **Watanabe S**, **Ando J**, **Iwadate M**, **Yamamoto M**, **Lee M-S**, **Tanaka K**, **Komatsu M**. Persistent activation of Nrf2 through p62 in hepatocellular carcinoma cells. *J Cell Biol* 193: 275–84, 2011.

23. **Iverson S V.**, **Comstock KM**, **Kundert JA**, **Schmidt EE**. Contributions of new hepatocyte lineages to liver growth, maintenance, and regeneration in mice. *Hepatology* 54: 655–63, 2011.

24. **Jin L**, **Long L**, **Green MA**, **Spear BT**. The alpha-fetoprotein enhancer region activates the albumin and alpha-fetoprotein promoters during liver development. *Dev Biol* 336: 294–300, 2009.

25. **Kim KH**, **Jeong YT**, **Oh H**, **Kim SH**, **Cho JM**, **Kim Y-N**, **Kim SS**, **Kim DH**, **Hur KY**, **Kim HK**, **Ko T**, **Han J**, **Kim HL**, **Kim J**, **Back SH**, **Komatsu M**, **Chen H**, **Chan DC**, **Konishi M**, **Itoh N**, **Choi CS**, **Lee M-S**. Autophagy deficiency leads to protection from obesity and insulin resistance by inducing Fgf21 as a mitokine. *Nat Med* 19: 83–92, 2013.

26. **Kim KH**, **Lee M-S**. Autophagy--a key player in cellular and body metabolism. *Nat Rev Endocrinol* 10: 322–37, 2014.

27. **Kofman A V**, **Morgan G**, **Kirschenbaum A**, **Osbeck J**, **Hussain M**, **Swenson S**, **Theise ND**. Dose- and time-dependent oval cell reaction in acetaminophen-induced murine liver injury. *Hepatology* 41: 1252–61, 2005.

28. **Komatsu M**, **Waguri S**, **Ueno T**, **Iwata J**, **Murata S**, **Tanida I**, **Ezaki J**, **Mizushima N**, **Ohsumi Y**, **Uchiyama Y**, **Kominami E**, **Tanaka K**, **Chiba T**. Impairment of starvation-induced and constitutive autophagy in Atg7-deficient mice. *J Cell Biol* 169: 425–434, 2005.

29. **Kuma A**, **Matsui M**, **Mizushima N**. LC3, an autophagosome marker, can be incorporated into protein aggregates independent of autophagy: Caution in the

712 interpretation of LC3 localization. *Autophagy* 3: 323–328, 2007.

713 30. **Kuma A**, **Mizushima N**. Chromosomal mapping of the GFP-LC3 transgene in
714 GFP-LC3 mice. *Autophagy* 4: 61–2, 2008.

715 31. **Kwanten WJ**, **Martinet W**, **Michielsen PP**, **Francque SM**. Role of autophagy
716 in the pathophysiology of nonalcoholic fatty liver disease: A controversial issue.
717 *World J Gastroenterol* 20: 7325–7338, 2014.

718 32. **Ma D**, **Molusky MM**, **Song J**, **Hu C-R**, **Fang F**, **Rui C**, **Mathew A V**,
719 **Pennathur S**, **Liu F**, **Cheng J-X**, **Guan J-L**, **Lin JD**. Autophagy deficiency by
720 hepatic FIP200 deletion uncouples steatosis from liver injury in NAFLD. *Mol*
721 *Endocrinol* 27: 1643–1654, 2013.

722 33. **Martinet W**, **Schrijvers DM**, **Timmermans J-P**, **Bult H**, **De Meyer GRY**.
723 Immunohistochemical analysis of macroautophagy: recommendations and
724 limitations. *Autophagy* 9: 386–402, 2013.

725 34. **Martinet W**, **Timmermans J-P**, **De Meyer GRY**. Methods to assess autophagy
726 in situ-transmission electron microscopy versus immunohistochemistry.
727 *Methods Enzymol* 543: 89–114, 2014.

728 35. **Miyajima A**, **Tanaka M**, **Itoh T**. Stem/progenitor cells in liver development,
729 homeostasis, regeneration, and reprogramming. *Cell Stem Cell* 14: 561–574,
730 2014.

731 36. **Mizushima N**, **Yamamoto A**, **Matsui M**, **Yoshimori T**, **Ohsumi Y**. In vivo
732 analysis of autophagy in response to nutrient starvation using transgenic mice
733 expressing a fluorescent autophagosome marker. *Mol Biol Cell* 15: 1101–1111,
734 2004.

735 37. **Ni H-M**, **Woolbright BL**, **Williams J**, **Copple B**, **Cui W**, **Luyendyk JP**,
736 **Jaeschke H**, **Ding W-X**. Nrf2 promotes the development of fibrosis and
737 tumorigenesis in mice with defective hepatic autophagy. *J Hepatol* 61: 617–25,
738 2014.

739 38. **Oslowski CM**, **Urano F**. Measuring ER stress and the unfolded protein
740 response using mammalian tissue culture system. 1st ed. Elsevier Inc., 2011.

741 39. **Postic C**, **Magnuson M a.** DNA excision in liver by an albumin-Cre transgene
742 occurs progressively with age. *Genesis* 26: 149–150, 2000.

743 40. **Ravikumar B**, **Sarkar S**, **Davies JE**, **Futter M**, **Garcia-Arencibia M**, **Green-**
744 **Thompson ZW**, **Jimenez-Sanchez M**, **Korolchuk VI**, **Lichtenberg M**, **Luo S**,
745 **Massey DCO**, **Menzies FM**, **Moreau K**, **Narayanan U**, **Renna M**, **Siddiqi FH**,
746 **Underwood BR**, **Winslow AR**, **Rubinsztein DC**. Regulation of mammalian
747 autophagy in physiology and pathophysiology. *Physiol Rev* 90: 1383–435,
748 2010.

749 41. **Rosenfeldt MT**, **Nixon C**, **Liu E**, **Mah LY**, **Ryan KM**. Analysis of
750 macroautophagy by immunohistochemistry. *Autophagy* 8: 963–969, 2012.

751 42. **Rutkowski DT**, **Wu J**, **Back SH**, **Callaghan MU**, **Ferris SP**, **Iqbal J**, **Clark R**,
752 **Miao H**, **Hassler JR**, **Fornek J**, **Katze MG**, **Hussain MM**, **Song B**,
753 **Swathirajan J**, **Wang J**, **Yau GDY**, **Kaufman RJ**. UPR Pathways Combine to
754 Prevent Hepatic Steatosis Caused by ER Stress-Mediated Suppression of
755 Transcriptional Master Regulators. *Dev Cell* 15: 829–840, 2008.

43. **Senft D**, **Ronai ZA**. UPR, autophagy, and mitochondria crosstalk underlies the ER stress response. *Trends Biochem. Sci.* (February 2015). doi: 10.1016/j.tibs.2015.01.002.

44. **Shibata M**, **Yoshimura K**, **Furuya N**, **Koike M**, **Ueno T**, **Komatsu M**, **Arai H**, **Tanaka K**, **Kominami E**, **Uchiyama Y**. The MAP1-LC3 conjugation system is involved in lipid droplet formation. *Biochem Biophys Res Commun* 382: 419–23, 2009.

45. **Shoulders MD**, **Ryno LM**, **Genereux JC**, **Moresco JJ**, **Tu PG**, **Wu C**, **Yates JR**, **Su AI**, **Kelly JW**, **Wiseman RL**. Stress-Independent Activation of XBP1s and/or ATF6 Reveals Three Functionally Diverse ER Proteostasis Environments. *Cell Rep* 3: 1279–1292, 2013.

46. **Singh R**, **Kaushik S**, **Wang Y**, **Xiang Y**, **Novak I**, **Komatsu M**, **Tanaka K**, **Cuervo AM**, **Czaja MJ**. Autophagy regulates lipid metabolism. *Nature* 458: 1131–5, 2009.

47. **Takamura A**, **Komatsu M**, **Hara T**, **Sakamoto A**, **Kishi C**, **Waguri S**, **Eishi Y**, **Hino O**, **Tanaka K**, **Mizushima N**, **Figure S**. Autophagy-deficient mice develop multiple liver tumors. *Genes Dev* 25: 795–800, 2011.

48. **Teske BF**, **Baird TD**, **Wek RC**. Methods for analyzing eIF2 kinases and translational control in the unfolded protein response. *Methods Enzymol* 490: 333–56, 2011.

49. **Tian Y**, **Kuo C-F**, **Sir D**, **Wang L**, **Govindarajan S**, **Petrovic LM**, **Ou J-HJ**. Autophagy inhibits oxidative stress and tumor suppressors to exert its dual effect on hepatocarcinogenesis. *Cell Death Differ* 22: 1025–34, 2015.

50. **Torres DM**, **Williams CD**, **Harrison SA**. Features, diagnosis, and treatment of nonalcoholic fatty liver disease. *Clin Gastroenterol Hepatol* 10: 837–58, 2012.

51. **Vernon G**, **Baranova A**, **Younossi ZM**. Systematic review: the epidemiology and natural history of non-alcoholic fatty liver disease and non-alcoholic steatohepatitis in adults. *Aliment Pharmacol Ther* 34: 274–85, 2011.

52. **Wei Y**, **Pattingre S**, **Sinha S**, **Bassik M**, **Levine B**. JNK1-mediated phosphorylation of Bcl-2 regulates starvation-induced autophagy. *Mol Cell* 30: 678–88, 2008.

53. **Xiao X**, **Li J**, **Samulski RJ**. Production of high-titer recombinant adeno-associated virus vectors in the absence of helper adenovirus. *J Virol* 72: 2224–32, 1998.

54. **Xu X**, **So J-S**, **Park J-G**, **Lee A-H**. Transcriptional control of hepatic lipid metabolism by SREBP and ChREBP. *Semin Liver Dis* 33: 301–11, 2013.

55. **Yang L**, **Li P**, **Fu S**, **Calay ES**, **Hotamisligil GS**. Defective hepatic autophagy in obesity promotes ER stress and causes insulin resistance. *Cell Metab* 11: 467–78, 2010.

56. **Zhang X-Q**, **Xu C-F**, **Yu C-H**, **Chen W-X**, **Li Y-M**. Role of endoplasmic reticulum stress in the pathogenesis of nonalcoholic fatty liver disease. *World J Gastroenterol* 20: 1768–76, 2014.

FIGURES - LEGENDS

Fig. 1. Transmission electron microscopy (TEM) of the livers of *Atg7$^{+/+}$Alb-Cre^{+}* and *Atg7$^{F/F}$Alb-Cre^{+}* mice

(A) Early and late autophagic vacuoles (arrows) and lipid droplets (*) are demonstrated in *Atg7$^{+/+}$Alb-Cre^{+}* mice. In one of the autophagosomes there was also the inclusion of a lipid droplet (arrowhead). Scale bars 5μm (left), 1μm (right)

(B) In livers of *Atg7$^{F/F}$Alb-Cre^{+}* mice, autophagic vacuoles are lacking and (sometimes deformed) mitochondria (blank arrows) accumulated. Scale bar, 1μm

Fig. 2. Severe hepatomegaly in *Atg7$^{F/F}$Alb-Cre^{+}* mice, but not in *Atg7$^{+/+}$Alb-Cre^{+}* mice

(A) The body weight of *Atg7$^{+/+}$Alb-Cre^{+}* and *Atg7$^{F/F}$Alb-Cre^{+}* mice was not significantly different (p=0.098).

(B) Macroscopic view of an *Atg7$^{+/+}$Alb-Cre^{+}* (left) and *Atg7$^{F/F}$Alb-Cre^{+}* (right) mouse illustrating the prominent hepatomegaly in *Atg7$^{F/F}$Alb-Cre^{+}* mice.

(C) The hepatomegaly is also reflected by a significantly higher liver-to-body weight ratio in *Atg7$^{F/F}$Alb-Cre^{+}* mice (***p<0.001).

Fig. 3. Hepatic microscopic alterations in *Atg7$^{F/F}$Alb-Cre^{+}* mice

(A) Representative photographs of an HE-stain (left panels), reticulin stain (middle panels) and Picrosirius red stain (right panels) of *Atg7*$^{+/+}$*Alb-Cre*$^{+}$ (upper panels) and *Atg7*$^{F/F}$*Alb-Cre*$^{+}$ mouse liver sections (lower panels), illustrating the severely disturbed architecture of the liver cell plates with hepatocellular hypertrophy, increased fibrosis, thickened trabeculae and a disrupted arrangement of the trabeculae in *Atg7*$^{F/F}$*Alb-Cre*$^{+}$ mice. The arrow indicates an apoptotic body. Scale bars, 100 µm.

(B) Morphometric analysis of the Picrosirius red positive area. *Atg7*$^{F/F}$*Alb-Cre*$^{+}$ mice had a significantly larger positive area (Student's-t-test, **p<0.01).

(C) *Atg7*$^{F/F}$*Alb-Cre*$^{+}$ mice showed an increased number of α-SMA positive cells lining the sinusoids, indicative of hepatic stellate cell activation, whereas in *Atg7*$^{+/+}$*Alb-Cre*$^{+}$ mice solely the perivascular structures are positive. Scale bars, 100 µm.

(D) Alpha smooth muscle actin (αSMA) score. *Atg7*$^{F/F}$*Alb-Cre*$^{+}$ mice had a significantly higher total score (Mann-Whitney U test, ***p<0.001).

(E) Pronounced ductular reaction in *Atg7*$^{F/F}$*Alb-Cre*$^{+}$ mouse liver with neoductular formation (HE-stain, upper panels). The ductular reaction was confirmed by a pan-cytokeratin stain (lower panels) whilst in *Atg7*$^{+/+}$*Alb-Cre*$^{+}$ mice only bile ducts were stained (lower left panel). Detailed photographs of the two encircled regions of the middle panels are shown (right panels). Scale bars, 100 µm; detailed images, 50 µm.

(F) *Atg7*$^{F/F}$*Alb-Cre*$^{+}$ livers showed infiltration of lymphoid cells as demonstrated by a CD3-stain. Arrows indicate CD3-positive cells. Scale bars, 100 µm.

Fig. 4. Autophagy-deficiency differentially disturbs the UPR pathways

(A) RT-qPCR of *Atf6* and the chaperones involved in the ATF6 pathway. Relative mRNA expression was compared to *Atg7*$^{+/+}$*Alb-Cre*$^{+}$. Although *Atf6* expression itself was unaltered in *Atg7*$^{F/F}$*Alb-Cre*$^{+}$ mice, its associated chaperones were significantly decreased. (*p<0.05, **p<0.01)

(B) RT-qPCR of the downstream effectors of the PERK pathway *Chop* and *Gadd34*. *Chop* is responsible for the induction of ER stress induced apoptosis and was significantly upregulated in *Atg7*$^{F/F}$*Alb-Cre*$^{+}$ mice, while *Gadd34* was unaltered. (***p<0.001)

(C). Caspase-3 activity was significantly elevated in *Atg7*$^{F/F}$*Alb-Cre*$^{+}$ mice. (**p<0.01)

(D) RT-qPCR of *Ire1* and the chaperones involved in the IRE1α pathway. Relative mRNA expression was compared to *Atg7*$^{+/+}$*Alb-Cre*$^{+}$ mice. Neither *Ire1a* and its major effector *XBP1u,* nor activation of *XBP1u* to *XBP1s* was significantly altered in *Atg7*$^{F/F}$*Alb-Cre*$^{+}$ mice compared to controls. (***p<0.001)

(E) Western blot of several chaperones involved in the UPR. GAPDH was used as a loading control. Protein levels changed in line with the mRNA levels. Although the expression of *Atf6* was not significantly decreased, its phosphorylation was strongly attenuated in *Atg7*$^{F/F}$*Alb-Cre*$^{+}$ mice.

(F) Western blotting for SREBP-1 on whole cell and nuclear fractions.

(G) Densitometry analysis of the ratio of phosphorylated eIF2α to total eIF2α bands normalized to GAPDH and relative to control. (*p<0.05)

Fig. 5. Liver fat stains, ATG7 stain and transmission electron microscopy of *Atg7$^{F/F}$Alb-Cre^{+}* mice

(A) Oil-red-O (ORO) and Sudan Black B (SBB) stain demonstrated a fasting-induced steatosis in *Atg7$^{+/+}$Alb-Cre^{+}* mice (upper panels), whereas lipids were virtually absent in *Atg7$^{F/F}$Alb-Cre^{+}* mice (lower panels).

(B) Morphometric measurement of the ORO positive area confirmed the virtual absence of ORO-positive lipids in the *Atg7$^{F/F}$Alb-Cre^{+}* mice (Student's-t-test, *** $p<0.001$).

(C) Representative photographs of ORO and SBB positive grouped cells in *Atg7$^{F/F}$Alb-Cre^{+}* mice, which could be focally detected in the liver. These cells are mostly grouped around a larger droplet/vesicle, and contain a mixture of larger and smaller lipid droplets seemingly arranged around the nuclei and plasma membranes.

(D) Immunohistochemical staining with ATG7 confirms the knock-out of *Atg7* in *Atg7$^{F/F}$Alb-Cre^{+}* mice, with absent cytoplasmic staining in the hepatocytes compared to *Atg7$^{+/+}$Alb-Cre^{+}*. The darker cells in *Atg7$^{F/F}$Alb-Cre^{+}* mice compared to the surrounding cells, appear to correspond to the cells with (condensed cytoplasm) pro-apoptotic features on the HE-stain (see Fig 3A). Larger magnifications demonstrate the positivity on the non-hepatocytes (arrows), while the ductular reaction is negative as well (as these cells also express albumin; arrowheads). Scale bars, 100µm and 50µm.

(E) Transmission electron microscopy (TEM) of the livers of *Atg7$^{F/F}$Alb-Cre^{+}* mice. Some lipid containing cells could be detected. These cells not only contained lipid droplets, but also autophagic vacuoles, whilst lipid droplets and/or autophagosomes were not observed in the other hepatocytes. Arrows indicate autophagic vacuoles, asterisks (*) indicate lipid droplets. Scale bars, 1µm.

TABLES

Table 1. Characteristics of the antibodies used in the study.

Antigen	Antibody isotype, clone	Company	Cat no.
aSMA	Mouse monoclonal IgG, 1A4	Sigma-Aldrich	F3777
ATF6	Mouse monoclonal IgG1, 70B1413	Abcam	ab11909
ATG7	Rabbit polyclonal IgG	Sigma-Aldrich	A2856
ATG7	Rabbit polyclonal IgG	Santa Cruz	sc-33211
Beta-actin	Rabbit monoclonal IgG	Cell Signaling	#4970
CHOP	Mouse monoclonal IgG2a, L63F7	Cell Signaling	2895
eIF2α	Rabbit polyclonal IgG	Cell Signaling	9721
Phospho-eIF2α	Rabbit monoclonal IgG1, 119A11	Cell Signaling	3597
GADD34	Rabbit polyclonal IgG, H193	Santa Cruz	sc-8327
GAPDH	Rabbit polyclonal IgG	Abcam	ab9485
GRP78	Rabbit monoclonal IgG, C50B12	Cell Signaling	3177
Phospho-IRE1α	Rabbit polyclonal IgG	Novus Biological	nb100-2323
LC3B	Rabbit monoclonal IgG, D11	Cell Signaling	#3868
SQSTM1/p62	Rabbit polyclonal IgG	Sigma-Aldrich	P0067
pan-CK	Rabbit polyclonal IgG	DAKO	Z0622
PDIA4	Rabbit polyclonal IgG	Cell Signaling	2798
SREBP-1	Rabbit polyclonal IgG, C-20	Santa Cruz	Sc-366

The specificity, isotype, clone number, and catalog number of the antibodies are indicated if provided by the manufacturer. In case of ATG7, one antibody was used for Western blotting (Sigma-Aldrich), while the other antibody was used for immunohistochemistry (Santa Cruz).

Table 2. Primers used for real time PCR experiments.

Gene symbol	Reference sequence	Forward primer (5'-3')	Reverse primer (5'-3')	Efficiency	R^2
Atf6	NM_001081304.1	GGGCAGGGCCATTCTTGCTGA	AGCCCCCGGGACAAACAGGT	98.6	0.99
Calnexin	NM_001110499.1	CAACAGGGGAGGTTTATTTTGCT	TCCCACTTTCCATCATATTTGGC	101	0,99
Calreticulin	NM_007591.3	GGTGGCCGCGTCCGTCAATA	AGCAGGAGCGGCACCGAAAG	95.08	0.98
Chop	NM_007837.3	AGCGCAACATGACAGTGAAG	GTGTAATTCCAGGGGGAGGT	101.2	0.99
Dnajc3	NM_008929.3	GCTGAGTGTGGAGTAAATGCG	CGGCTGCGAGTAATTTCTTCC	103	0.99
Edem1	NM_138677.2	CTTGAGGGACCCCGACGGCT	TCTCAAGCCGCCCCTCCGTT	104	0.98
Erdj4	NM_013760.4	CGCCCTGTGGCCCTGACTTG	AGCTTTCAGGGGCAAACAGCCA	98.1	0.98
Gapdh	NM_008084.2	GCCGGCTCAGTGAGACAAG	TGGCACCTTCAGCAACAATG	95.1	0.99
Grp78	NM_001163434.1	TGCCGAGCTAAATTACACATTG	CCTTGTGGAGGGATGTACAGA	107.3	0.99
Grp94	NM_011631.1	GAGGCGGCTCCTGAGACCGAA	GGACCCTCATGGTGCGTGGC	101.2	0.99
Herpud1	NM_022331.1	ACGCCAAGTGTCGTTGTGTGGTC	GCTCGACTGCGCTCAGGGATG	92.8	0.99
Ire1	NM_023913.2	GCCCAACGCACATGGCAGGA	TACCCCTGAACGGCGGCTGA	98,6	0.99
Pdia3	NM_007952.2	GCAGGCCTAGGGGGTTGGGA	GAGGGCCGGGACCGGAGAAA	107.1	0.99
Pdia4	NM_009787.2	ACGAGACCCCGGCGTTCGGA	TGGCACTTTGAGGAGGTGAGCC	90.6	0.99
Xbp1s	NM_013842.2	TCTCAAGCCGCCCCTCCGTT	CGGGGTTGCTGGTGTGCCAT	97.6	0.98
Xbp1u	NM_013842.2	TCTCAAGCCGCCCCTCCGTT	GTGGCTGGCGTGCAAGGGAT	107.3	0.97

The references and primer sequences of the analyzed genes. The PCR-efficiency of each primer pair was calculated using a standard curve of reference cDNA. Amplification efficiency R^2 was determined using the formula 10-1/slope.

902 **Table 3. Biochemical plasma analyses**

903

	Atg7$^{+/+}$Alb-Cre^{+}			*Atg7$^{F/F}$Alb-Cre^{+}*			
	n	**Mean ± SEM**	***Range (min-max)***	**n**	**Mean ± SEM**	***Range (min-max)***	**p-value**
AST (U/L)	15	175.1 ± 22.4	*60.2 – 360.7*	10	1855.1 ± 279.9	*770.0 – 3636.0*	***
ALT (U/L)	15	20.1 ± 2.6	*8.0 – 42.3*	10	737.7 ± 146.2	*168.3 – 1682.0*	***
ALP (U/L)	15	127.6 ± 8.2	*78.3 – 203.4*	10	335.7 ± 12.5	*283.8 – 383.2*	***
GGT (U/L)	15	5.6 ± 0.2	*5.0 – 6.6*	10	14.4 ± 0.7	*12.0 – 18.7*	***
Total cholesterol (mg/dL)	15	73.5 ± 4.1	*50.0 – 97.4*	10	140.8 ± 8.2	*96.5 – 171.9*	***
HDL cholesterol (mg/dL)	15	63.5 ± 5.2	*6.6 – 87.8*	9	129.3 ± 7.6	*88.5 – 150.0*	***
LDL cholesterol (mg/dL)	15	6.6 ± 0.8	*2.9 – 16.0*	10	12.8 ± 2.1	*1.0 – 19.8*	*
LDL/HDL ratio	15	0.2 ± 0.2	*0.03 – 2.42*	9	0.1 ± 0.0	*0.01 – 0.15*	0.46
Triglycerides (mg/dL)	15	67.9 ± 7.7	*40.2 – 121.6*	10	15.1 ± 3.8	*3.0 – 39.1*	***
Glucose (mg/dL)	15	106.9 ± 5.7	*80.7 – 144.7*	10	87.4 ± 6.4	*54.8 – 115.1*	*
Insulin (ng/mL)	16	0.3 ± 0.0	*0.2 – 0.7*	11	0.3 ± 0.0	*0.2 – 0.4*	0.54

904

905 Main characteristics of autophagy-competent (*Atg7$^{+/+}$Alb-Cre^{+}*) and autophagy-
906 deficient (*Atg7$^{F/F}$Alb-Cre^{+}*) mice. Sample size (n) varies depending on the plasma
907 volume available for each mouse.
908 AST, aspartate transaminase; ALT, alanine transaminase; GGT, gamma-glutamyl
909 transferase; ALP, alkaline phosphatase

Fig. 1

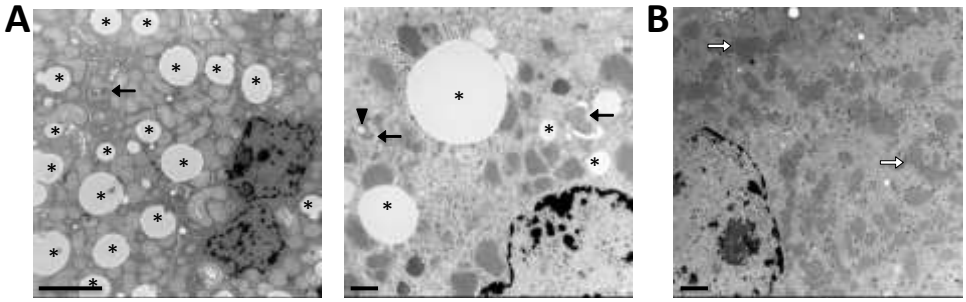

910

Fig. 2

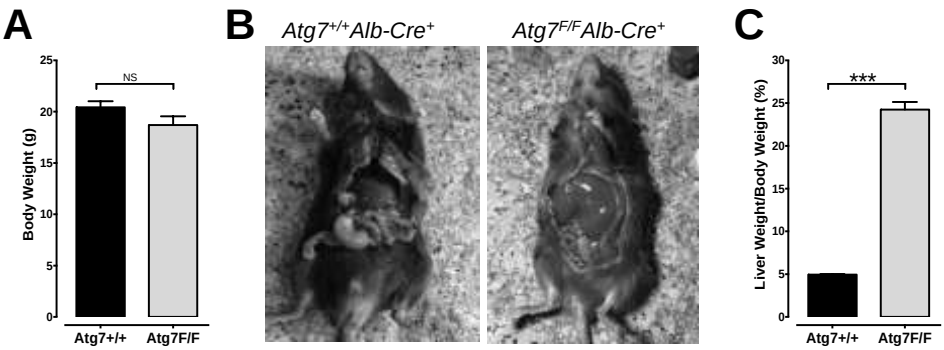
A
B
C
Atg7+/+Alb-Cre+
Atg7F/FAlb-Cre+
NS
Body Weight (g)
25
20
15
10
5
0
Atg7+/+
Atg7F/F
***
Liver Weight/Body Weight (%)
30
25
20
15
10
5
0
Atg7+/+
Atg7F/F

911

Fig. 3

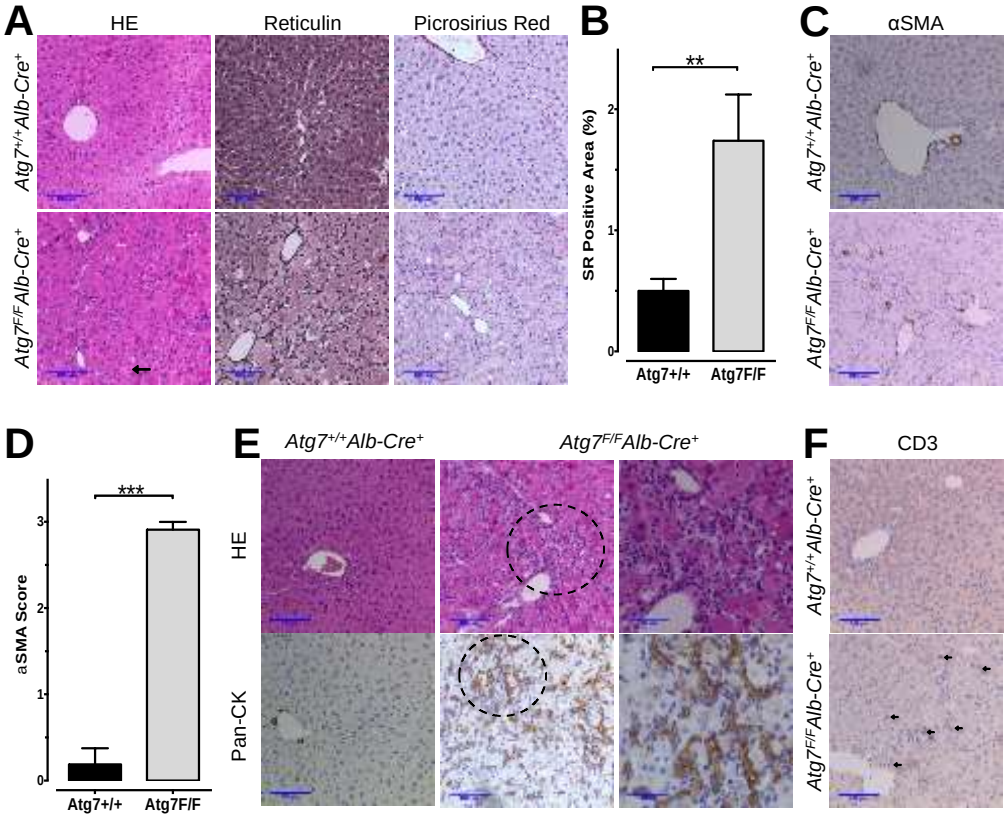
A
HE
Reticulin
Picrosirius Red
Atg7+/+Alb-Cre+
Atg7F/FAlb-Cre+
B
SR Positive Area (%)
**
Atg7+/+
Atg7F/F
C
αSMA
D
αSMA Score
***
E
Atg7+/+Alb-Cre+
Atg7F/FAlb-Cre+
HE
Pan-CK
F
CD3

912

Fig.4

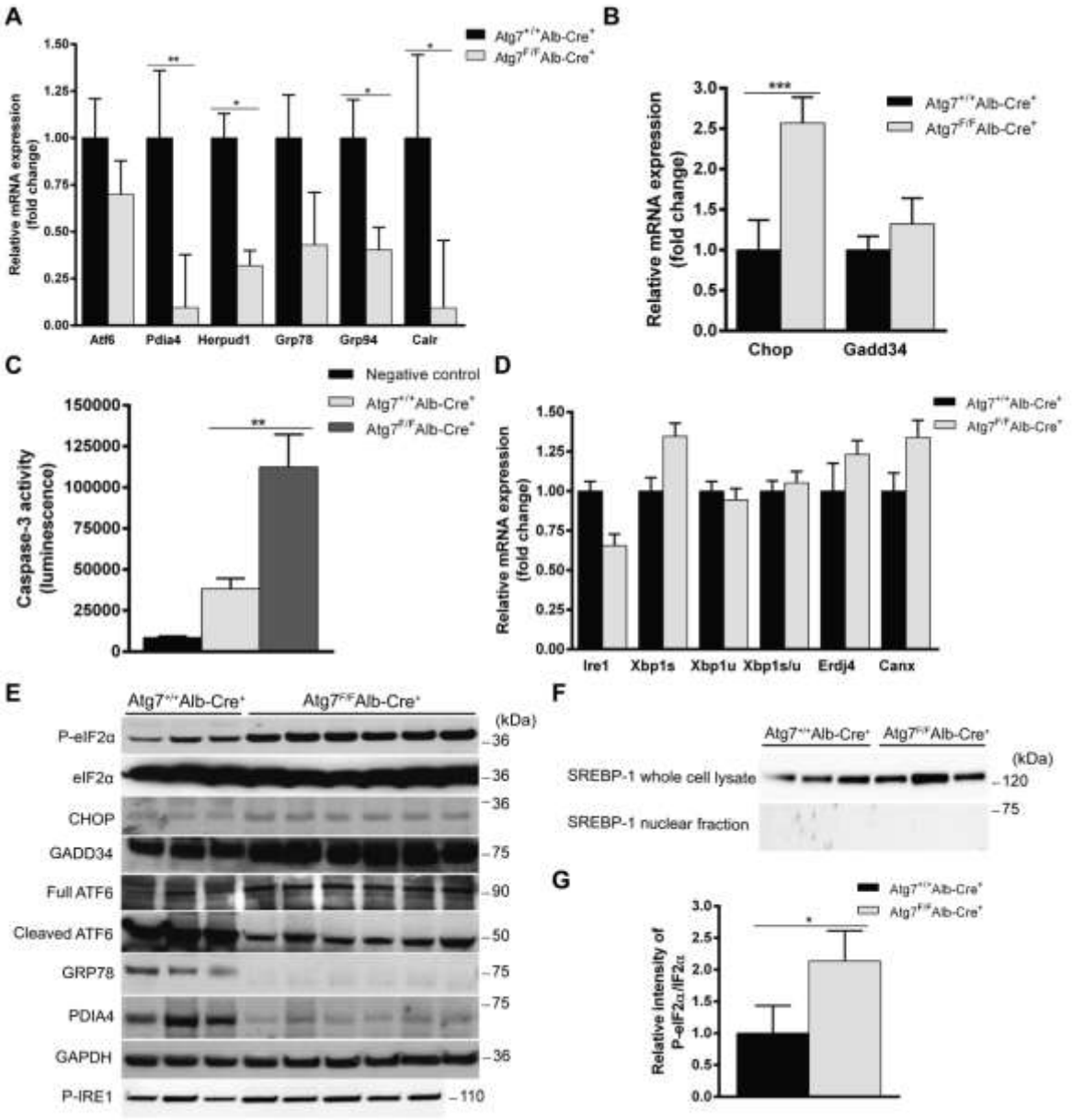
A
Relative mRNA expression (fold change)
Atg7+/+Alb-Cre+
Atg7F/FAlb-Cre+
Atf6
Pdia4
Herpud1
Grp78
Grp94
Calr
B
Relative mRNA expression (fold change)
Chop
Gadd34
C
Caspase-3 activity (luminescence)
Negative control
D
Relative mRNA expression (fold change)
Ire1
Xbp1s
Xbp1u
Xbp1s/u
Erdj4
Canx
E
(kDa)
P-eIF2α
eIF2α
CHOP
GADD34
Full ATF6
Cleaved ATF6
GRP78
PDIA4
GAPDH
P-IRE1
F
SREBP-1 whole cell lysate
SREBP-1 nuclear fraction
G
Relative intensity of P-eIF2α/IF2α

913

Fig. 5

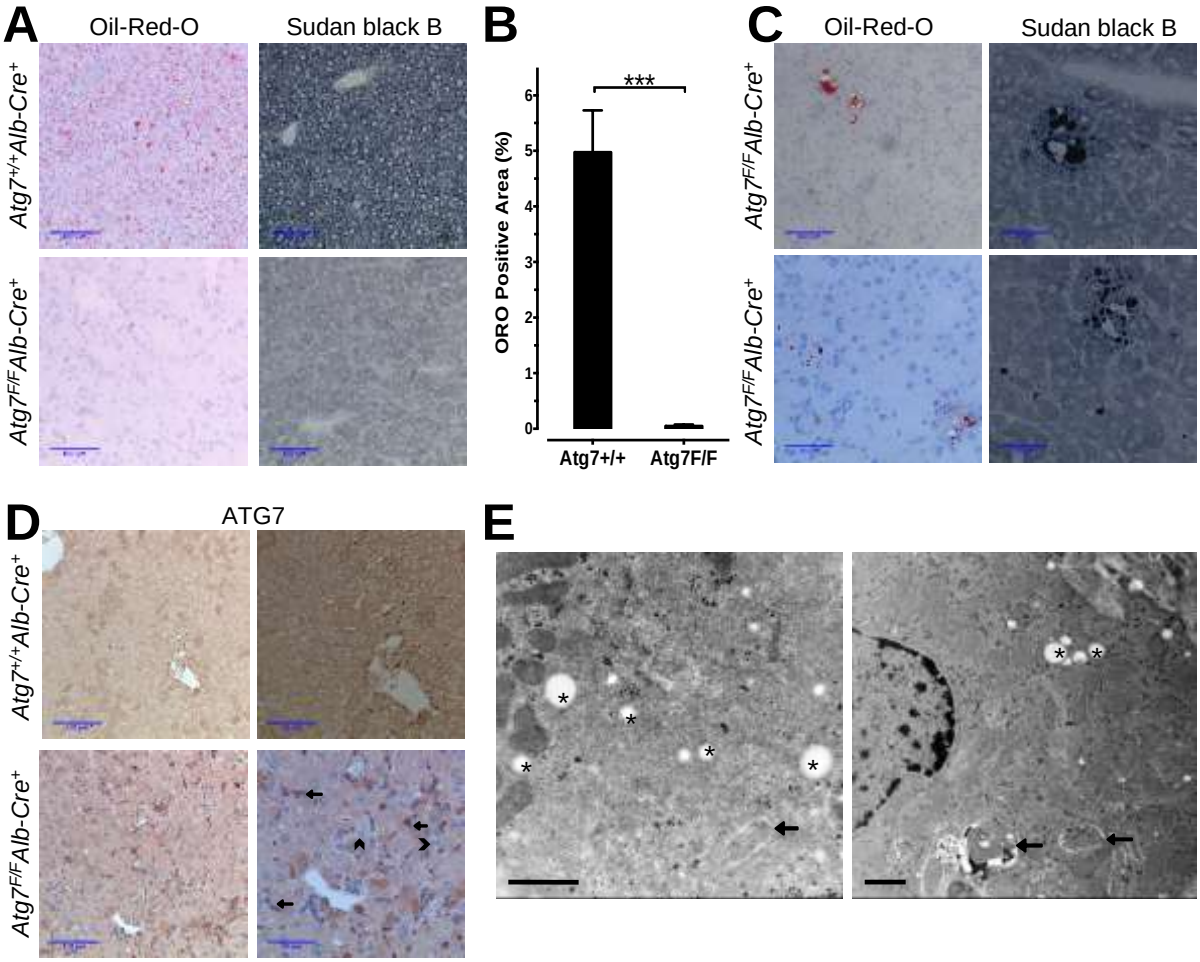
A
Oil-Red-O
Sudan black B
Atg7+/+Alb-Cre+
Atg7F/FAlb-Cre+
B
ORO Positive Area (%)
***
Atg7+/+
Atg7F/F
C
Oil-Red-O
Sudan black B
Atg7F/FAlb-Cre+
Atg7F/FAlb-Cre+
D
ATG7
Atg7+/+Alb-Cre+
Atg7F/FAlb-Cre+
E

914

SUPPLEMENTARY MATERIAL

TITLE

Hepatocellular autophagy modulates the unfolded protein response and fasting-induced steatosis in mice

AUTHORS

Wilhelmus J. Kwanten[1], Y.-P. Vandewynckel[2], Wim Martinet[3], Benedicte Y. De Winter[1], Peter P. Michielsen[1,4], Viviane Van Hoof[5], Ann Driessen[6], Jean-Pierre Timmermans[7], Pierre Bedossa[8], Hans Van Vlierberghe[2], Sven M. Francque[1,4]

Figure S1. Validation of hepatocyte-specific autophagy-deficiency by Western blot and immunohistochemistry of $Atg7^{+/+}$Alb-Cre^{+} and $Atg7^{F/F}$Alb-Cre^{+} mice.

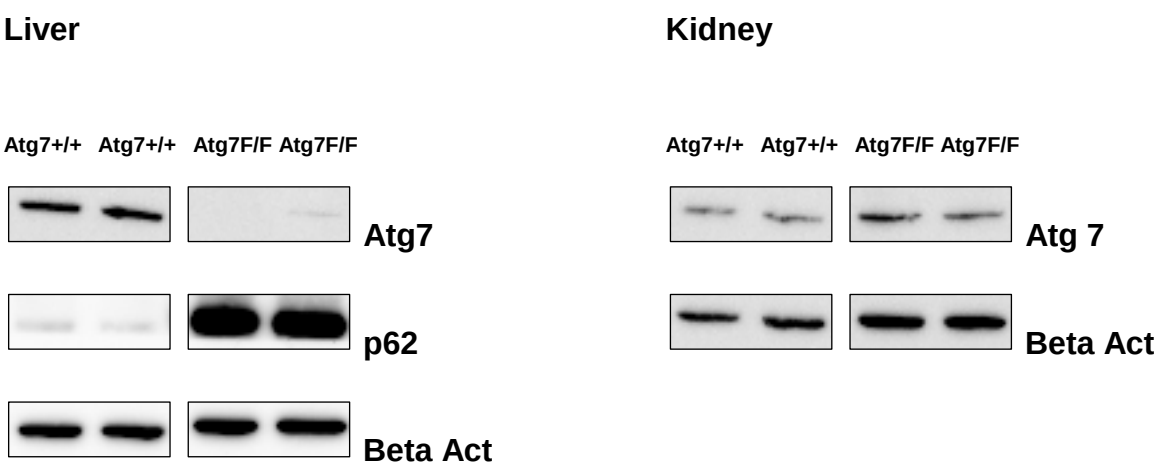

(A) Western blot of the liver and kidneys of $Atg7^{+/+}$Alb-Cre^{+} and $Atg7^{F/F}$Alb-Cre^{+} mice. The autophagy gene *Atg7,* indispensible for the initiation of autophagy, was successfully deleted in the liver of $Atg7^{F/F}$Alb-Cre^{+} mice, but not in kidney. The protein SQSMT1/p62, which is degraded by autophagy, accumulates correspondingly in the livers of $Atg7^{F/F}$Alb-Cre^{+} mice.

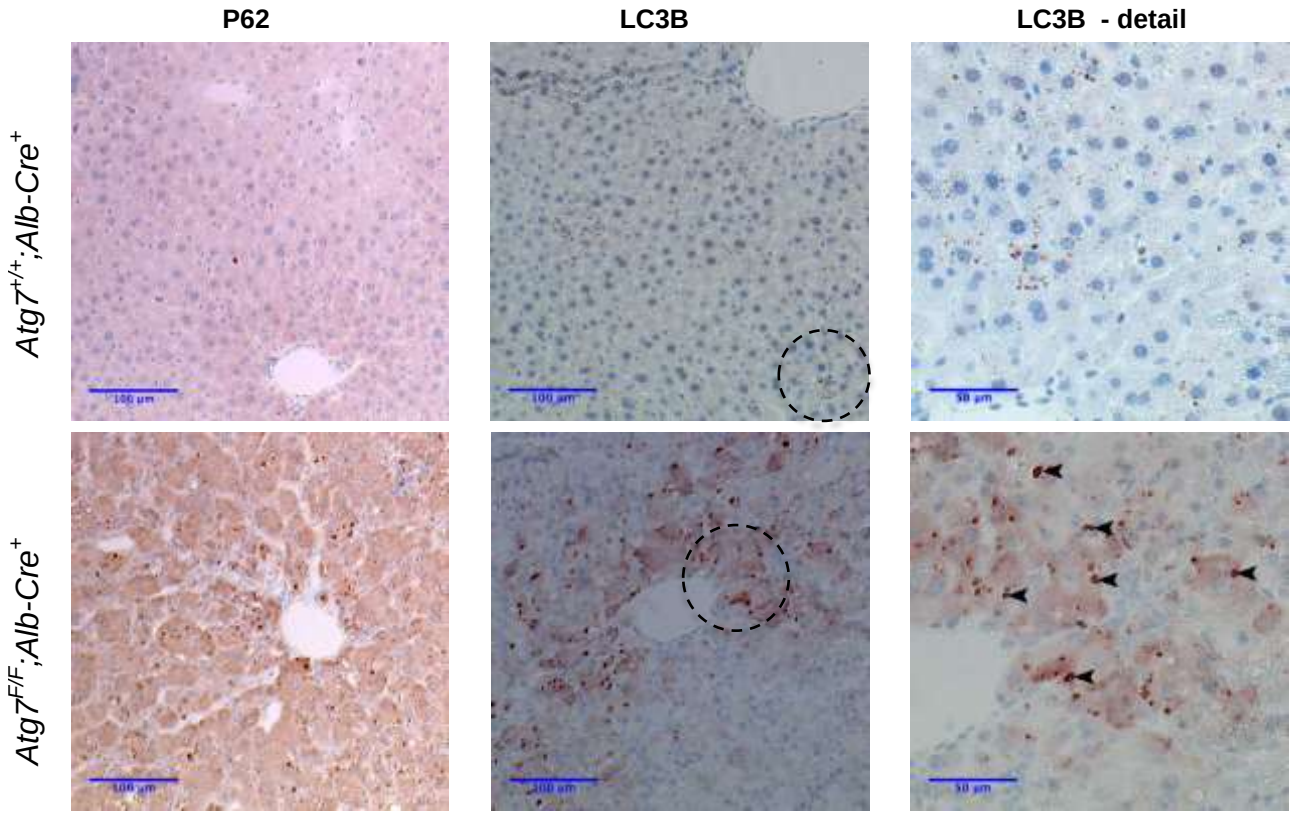

(B) Immunohistochemical analysis of livers sections of *Atg7*$^{+/+}$*Alb-Cre*$^{+}$ (upper panels) and *Atg7*$^{F/F}$*Alb-Cre*$^{+}$ mice (lower panels). *Atg7*$^{F/F}$*Alb-Cre*$^{+}$ mice show accumulation of p62 positive aggregates, whereas this is not the case in autophagy-competent *Atg7*$^{+/+}$*Alb-Cre*$^{+}$ mice. An LC3B-stain reveals sparsely fine positive punctae in *Atg7*$^{+/+}$*Alb-Cre*$^{+}$ mice, representing autophagosomes. Autophagy-deficient *Atg7*$^{F/F}$*Alb-Cre*$^{+}$ mice lack these fine punctae. However, they show cytoplasmic positivity and large positive globular structures (arrowheads) predominantly in the pericentral regions, representing staining of the unconjugated GFP-bound LC3-I protein, which can be incorporated in protein aggregates autophagy-independently. Detailed photographs of the encircled regions are shown in the right panels.